

## Effects of $\text{Cd}^{2+}$ on the epithelial $\text{Na}^+$ channel (ENaC) investigated by experimental and modeling studies

Maria Mernea<sup>1</sup>, Roxana Ulăreanu<sup>1</sup>, Octavian Călborean<sup>1</sup>, Sergiu Chira<sup>2</sup>, Octavian Popescu<sup>2</sup>, Dan F. Mihailescu<sup>1</sup> and Dana Cucu<sup>1</sup>

<sup>1</sup> Department of Anatomy, Physiology and Biophysics, Faculty of Biology, University of Bucharest, Bucharest, Romania

<sup>2</sup> Molecular Biology Centre, Institute for Interdisciplinary Experimental Research, University “Babes-Bolyai”, 42 August Treboniu Laurean, 400271 Cluj-Napoca, Romania

**Abstract.** The function of the epithelial  $\text{Na}^+$  channel from the apical membrane of many  $\text{Na}^+$  transporting epithelia is modulated by various chemical compounds from the extracellular space, such as heavy metals, protons or chloride ions. We have studied the effect of extracellular  $\text{Cd}^{2+}$  on the function of the epithelial  $\text{Na}^+$  channel (ENaC) in heterologously expressed *Xenopus laevis* oocytes and  $\text{Na}^+$ -transporting epithelia. We assayed channel function as the amiloride-sensitive sodium current ( $I_{\text{Na}}$ ).  $\text{Cd}^{2+}$  rapidly and voltage-independently inhibited  $I_{\text{Na}}$  in oocytes expressing  $\alpha\beta\gamma$  *Xenopus* ENaC (xENaC). The extracellular  $\text{Cd}^{2+}$  inhibited  $\text{Na}^+$  transport and showed no influence on ENaC trafficking, as revealed by concomitant measurements of the transepithelial current, conductance and capacitance in  $\text{Na}^+$ -transporting epithelia. Instead, amiloride inhibition was noticeably diminished in the presence of  $\text{Cd}^{2+}$  on the apical membrane. Using molecular modeling approaches, we describe the amiloride binding sites in rat and xENaC structures, and we present four putative binding sites for  $\text{Cd}^{2+}$ . These results indicate that ENaC functions as a sensor for external  $\text{Cd}^{2+}$ .

**Key words:** ENaC — *Xenopus laevis* —  $\text{Cd}^{2+}$  — A6 epithelia

### Introduction

Cadmium has been described as one of the most harmful pollutants since the 19th century, when exposure to cadmium was seen as a problem confined especially to occupational exposure.

Today, it is widely accepted that the main source of cadmium is cigarette smoke. This source and the accumulation of the metal in tissues and organs are the concerns of the modern world. New data from the genomic era show that cadmium affects the human and animal genome with effects relevant to tumorigenesis, tumor development and many other countless

insults to human and animal organs (reviewed in Thevenod et al. 2013). The current theory suggests that cadmium has no direct genotoxic effects but rather a multitude of combined mechanisms leading to the dysregulation of cellular events such as cell growth, apoptosis and proliferation.

From the start of toxicology studies, the kidney was identified as the critical organ in cadmium exposure in humans and animals, and acute cytotoxic effects were related to tubular damage (Nordberg et al. 2009). Tubular damage was indicated to follow from oxidative stress (Cucu et al. 2011), affecting the vectorial active transport (Bathula et al. 2008) or damaging the epithelial barrier (Boveri et al. 2004). These processes were associated with the impaired function of various renal transporters. For instance, the ionic form of cadmium blocks the currents through the epithelial  $\text{Ca}^{2+}$  channel (ECaC), heterologously expressed in HEK cells (Vennekens et al. 2001), whereas cadmium-methallothionein-1 (Cd-MT) directly blocks the apical  $\text{Na}^+$ -glucose cotransporter on the luminal side in the proximal tubule (Tsuruoka et al. 2008). In the proximal tubular brush border,  $\text{Cd}^{2+}$  inhibits the transport of the inorganic sulfate

**Electronic supplementary material.** Figures S1, S2 and S3. The online version of this article (doi:10.4149/gpb\_2015054) contains supplementary material, which is available to authorized users.

Correspondence to: Dana Cucu, Department of Anatomy, Physiology and Biophysics, Faculty of Biology, University of Bucharest, Bucharest, Romania  
E-mail: dana.cucu@bio.unibuc.ro

(Si) or phosphate (Pi)<sup>+</sup> by blocking the NaSi-I cotransporter (Markovich and Knight 1998) and the NaPi-II transporter (Wagner et al. 1996; Park et al. 1997). These effects suggest that Cd<sup>2+</sup>-induced nephropathy relates to membrane transporters or ion channels (Barbier et al. 2004).

The amiloride-sensitive epithelial Na<sup>+</sup> channel (ENaC) participates in Na<sup>+</sup> reabsorption in the distal tubule and modulates the movement of heavy metals from the luminal or basolateral side of the epithelial cells. Data published to date have described the effects of trace elements such as Ni<sup>2+</sup>, Zn<sup>2+</sup>, Pb<sup>2+</sup> or Hg<sup>2+</sup> on native ENaC from kidney cells (Yu et al. 2007) or heterologously expressed channels in *Xenopus laevis* oocytes (Sheng et al. 2002; Amuzescu et al. 2003; Cucu et al. 2005). Interestingly, the effect of each of these metals depended on the species from which ENaC originated. For instance, Ni<sup>2+</sup> stimulated ENaC derived from *Xenopus laevis* kidney cells but inhibited the channel from rat colon (Cucu et al. 2005). Similarly, Zn<sup>2+</sup> inhibited ENaC from A6 epithelial cells and rat colon (Amuzescu et al. 2003) but stimulated ENaC derived from mouse kidney (Sheng et al. 2004). All together, these data reveal that ENaC is a true sensor for environmental pollutants, although the exact site(s) for metal binding are only poorly described.

Moreover, heavy metals can be used as tools in mutagenesis analysis to investigate the structural architecture of ENaC. Indeed, using Cd<sup>2+</sup> as a trace element, some groups have revealed important sites in channel conduction and selectivity filtering (Takeda et al. 2007), whereas Ni<sup>2+</sup> helped us to understand an important site in amiloride binding (Sheng et al. 2002; Cucu et al. 2005).

In line with our previous work, this study intends to use the modulation of *Xenopus* ENaC (xENaC) by Cd<sup>2+</sup> to elucidate new insights regarding the architecture of the ENaC channel. In contrast to rat ENaC, which appears to be externally insensitive to Cd<sup>2+</sup>, we provide evidence that Cd<sup>2+</sup> inhibits whole-cell currents in oocytes expressing  $\alpha\beta\gamma$  xENaC with an IC<sub>50</sub> in the  $\mu$ M range. Lacking three-dimensional structural data, we perform normal mode analysis of xENaC using the first solved crystal structure of the acid-sensing ion channel (ASIC1), a member of the same DEG/ENaC family. Molecular modeling allows the assumption that the Cd<sup>2+</sup> binding site is located in the extracellular loop of the  $\alpha$  rENaC subunit. Moreover, we predict four Cd<sup>2+</sup> binding sites in the  $\alpha$  xENaC structure. These sites, denoted CD1, CD2 CD3 and CD4, are located in the finger and thumb domains.

## Materials and Methods

### Oocyte isolation and injection

Oocytes in stage V-VI of development were surgically removed from a mature female *Xenopus laevis* (African

*Xenopus* facility, Knysna, RSA) anesthetized by immersion in tricaine methanesulfonate. After defolliculation in collagenase type V (1 mg/ml for 2 hours), the oocytes were stored in high-Na<sup>+</sup> solution. Healthy oocytes were then injected with 100 nl of a solution containing equal amounts of  $\alpha$ ,  $\beta$ , and  $\gamma$  ENaC subunits at a total concentration of 100 ng/ $\mu$ l.

Each subunit clone was linearized prior to *in vitro* transcription. The cRNA was synthesized using the RiboMAX<sup>TM</sup> Large Scale RNA Production System, SP6 (Promega, US) and purified using the SV Total RNA Isolation System (Promega, US).

ENaC-injected oocytes were stored in low-Na<sup>+</sup> storage solution. Experiments were performed between 24–72 hours after the injection of  $\alpha\beta\gamma$  xENaC expressing oocytes. All experiments were performed at room temperature (~20°C).

### Two-microelectrode voltage clamp measurements

Measurements were performed under voltage-clamp conditions by placing the oocytes in a recording chamber (RC-3Z, Warner Instruments, Hamden US). Oocytes were impaled with two microelectrodes filled with 3 M KCl exhibiting a resistance of 1–3 M $\Omega$ . Two Ag/AgCl pellets were used as bath electrodes. The electrodes were connected to a voltage-clamp amplifier (OC-725C, Warner Instruments, Hamden, USA). A fast-step perfusion system (VC-6 l perfusion valve controller Warner Instruments, Hamden, US) was used to deliver Cd<sup>2+</sup> and amiloride. Amiloride-sensitive currents are defined as the difference between the total currents and the currents with 10  $\mu$ M amiloride in the bath solution.

To minimize Na<sup>+</sup> influx and current rundown, whole-cell currents were recorded using oocytes clamped at 0 mV, the equilibrium potential in our working conditions (100 mM NaCl, 1 mM CaCl<sub>2</sub>, 3 mM KCl, 5 mM HEPES). CdCl<sub>2</sub> and amiloride were administered for one minute at holding potential prior to the application of voltage pulses. Currents obtained after subtraction of the amiloride-insensitive component obtained in 10  $\mu$ M amiloride are denoted amiloride-sensitive currents.

For current-voltage (IV) curves, oocytes were pulsed for 500 ms from –140 to +40 mV in 20 mV increments.

### Analysis of Cd<sup>2+</sup> effect in oocytes expressing ENaC

Short pulses of –60 mV were applied from 0 mV.

The dose-response relationship for the Cd<sup>2+</sup> inhibition of ENaC currents was obtained by plotting the relative currents measured at –60 mV with increasing concentrations of CdCl<sub>2</sub> (0.1, 5, 10, 100, 500, 1000 and 2000  $\mu$ M) against Cd<sup>2+</sup> concentrations using a semi-logarithmic scale. The relative currents (IR) represent the ratios of whole-cell amiloride-sensitive Na<sup>+</sup> currents in the presence of Cd<sup>2+</sup> in bath solutions relative to the current measured before Cd<sup>2+</sup>

application (control conditions). For the amiloride dose response, the relative currents represent the ratio between currents in the presence and in the absence of the inhibitor.

Non-linear least squares curve fitting was used to obtain the dose-response parameters. Dose-response data were fitted with the Hill equation using OriginPro 8.0 for Windows (OriginLabCorp., Northampton, MA) software. The equation is as follows:

$$IR = C^{n_H} / (IC_{50}^{n_H} + C^{n_H}) \quad (1)$$

where IR is the relative current in the presence of the inhibitor; IC<sub>50</sub> represents the concentration at 50% inhibition; C is the concentration of the inhibitor; and  $n_H$  represents the Hill coefficient. The total number of oocytes tested for the whole dose response curve is n.

#### A6 epithelia

A6 cells were kindly provided by Professor Willy van Driessche (Catholic University of Leuven, Belgium). They were grown on permeable Anopore filters (pore size 0.2 μm; Nunc Intermed, Roskilde, Denmark) at 28°C and 1% CO<sub>2</sub> in a humidified incubator. The growth medium consisted of a 1:1 mixture of Leibovitz's L-15 and Ham's F-12 media, supplemented with 10% fetal bovine serum (Gibco-Invitrogen, Carlsbad, US), 2.6 mM NaHCO<sub>3</sub>, 3.8 mM glutamine, 95 IU/ml penicillin and 95 μg/ml streptomycin, and was renewed twice weekly. We used cell passages 109–113, which were cultured between 12 to 30 days. The number of A6 epithelia used for an experimental protocol is expressed as N.

#### Transepithelial current, conductance capacitance measurements

A6 epithelia grown on Anopore inserts were mounted in a horizontal modified Ussing chamber (EP-devices, Bertem, BE) and continuously bathed with solution containing 100 mM NaCl, 3 mM KCl, 1 mM CaCl<sub>2</sub>, and 5 mM HEPES, pH = 7.4; osmolarity = 200 mosmol/kgH<sub>2</sub>O. After placement of the insert electrodes [agar bridged (3% in 3 M KCl) Ag-AgCl], the epithelium was voltage clamped at 0 mV. The hardware for impedance analysis was based on a digital signal-processing (DSP) board (model 310B, Dalanco Spry, Rochester, NY) connected to a personal computer. The interface between the DSP boards and the high-speed voltage clamp consisted of antialiasing filters, programmable gain amplifiers, and digital control circuits controlled by the DSP board (EP-devices, Bertem, BE). For the measurement of the transepithelial conductance ( $G_T$ ) and the transepithelial capacitance ( $C_T$ ), impedance spectra were obtained while the  $I_{sc}$  signals were interrupted. The estimation of transepithelial capacitance is based on the principle that a high-resistance

epithelium can be modeled as a simple “lumped” model. Therefore, impedance spectra were analyzed using a custom-made program (EP-devices, Bertem, BE) that enabled the impedance spectra to be fitted to a one membrane equivalent circuit model based on the results presented as Nyquist plots (Van Driessche et al. 2007). Amiloride at 100 μM was added on the apical side at the end of the experiment to estimate the amiloride-sensitive current ( $I_{Na}$ ).

#### Solution and chemicals

For the storage of un-injected oocytes, we used a high-Na<sup>+</sup> solution containing 90 mM NaCl, 2 mM KCl, 5 mM HEPES, and 2 mM CaCl<sub>2</sub> (pH 7.4). For the low-Na<sup>+</sup> solution, in which ENaC-injected oocytes were stored, 90% of the NaCl was replaced with N-methyl-D-glucamine (NMDG)-Cl. The recording solution for oocytes was 100 mM NaCl solution containing 100 mM NaCl, 3 mM KCl, 1 mM CaCl<sub>2</sub> and 5 mM HEPES, pH 7.4 adjusted with NaOH. Experiments performed in this solution are denoted controls (CTRL) in the figures. Where appropriate, Cd<sup>2+</sup> was added from a freshly prepared stock solution in 100 mM NaCl solution. All chemicals used in this study were purchased from Sigma (St. Louis, MO, USA).

#### Statistics

Data presented are averages ± SEM; n represents the number of experiments included. To analyze saturation curves, a nonlinear regression was fitted to a Hill equation using OriginLab version 8. Differences in Cd<sup>2+</sup> effects were tested for significance using the Student-*t* test, and  $p \leq 0.05$  was considered significant.

#### Modeling

Structural models of the trimeric αβγ rat (rENaC), *Xenopus* (xENaC) and human ENaC were built with MODELLER v9.11 software (Eswar et al. 2006). The extracellular loops of the α, β and γ rENaC and xENaC subunits were modeled using the template of the extracellular loop of a mouse ENaC, as previously described by Kashlan et al. (2011). The transmembrane (TM) regions were built based on the TM region of chicken ASIC1 in complex with psalmotoxin 1 at low pH (PDB code 4FZ0 (Bacongus and Gouaux 2012)). However, the ASIC1 TM helices in the 4FZ0 structure are incomplete. Therefore, the amino acids with no homology to the ASIC1 structure were constrained to adopt a helical conformation following to the direction of the ASIC1 helices. Sequence alignment was performed using Clustal W (Larkin et al. 2007) and manually adjusted based on previous mutagenesis studies (Supplementary Fig. S1).

Refined models were obtained by applying the titration state of amino acids at pH 7.4 as predicted with PROPKA (Li

et al. 2005). ENaC models were glycosylated with 21 N-acetylglucosamine (NAG) residues. These residues were attached at sites previously determined by experiments (Canessa et al. 1994; Snyder et al. 1994) or at predicted glycosylated sites (Consortium, The UniProt, 2012) using CHARMM (Brooks et al. 2009) with the CHARMM 36 topology and parameter files (MacKerell et al. 1998, 2003; Guvench et al. 2008; Best et al. 2012). Protonated amino acids and the glycosylation sites are highlighted on the sequence alignment in Fig. S1.

The pore radius of the refined models was determined using the HOLE2 (Smart et al. 1993) software. The electrostatic energy distribution was determined using the APBS (Baker et al. 2001) software, based on the ionic strength of the external solution (see *Solution and chemicals* section) and the maximal 2 mM concentration of  $\text{CdCl}_2$  used in the experiments.

Energy minimization and subsequent amiloride docking were performed using the ArgusLab 4.0.1 software (Thompson 2004). The coordinates of amiloride were retrieved from the DrugBank database (Nutter-Upham et al. 2008), and the molecule was placed in the vicinity of the extracellular putative amiloride binding site of the  $\alpha$  subunit, namely residues W278–Y283 of rENaC (Kelly et al. 2003) and their homologous residues W211–216 of xENaC, both ranges located on an  $\alpha$  helix. Prior to applying the docking procedures, the structures with amiloride were energy minimized. A better sampling of the amiloride binding site was performed using seven different orientations of amiloride with respect to this  $\alpha$  helix. The resulting poses were scored using the empirical scoring function AScore, and we analyzed only the top ten poses in detail. A similar approach was used to sample the second amiloride binding site (Kellenberger et al. 2003), positioned nearly in the center of the lipid bilayer.

## Results and Discussion

### Extracellular $\text{Cd}^{2+}$ modulates xENaC currents

The effect of extracellular  $\text{Cd}^{2+}$  was studied on  $\alpha\beta\gamma$  xENaC heterologously expressed in *Xenopus laevis* oocytes.

Oocytes expressing  $\alpha\beta\gamma$  xENaC were clamped at a holding potential of 0 mV and tested at voltage-steps ranging from  $-140$  to  $+40$  mV in 20 mV increments. Pulses were applied for 500 ms at 1 Hz. In Fig. 1, the averaged IV relationship of the currents for oocytes expressing  $\alpha\beta\gamma$  xENaC ( $n = 11$ ) are plotted in the absence (open circles) and in the presence of  $100 \mu\text{M}$   $\text{CdCl}_2$  (closed circles) and with  $10 \mu\text{M}$  amiloride in the bath solution (solid squares). This result indicates a direct inhibition of the channel by  $\text{Cd}^{2+}$ . The pulse potentials had no significant impact on the effect of  $\text{Cd}^{2+}$ , with approximately 50% inhibition of the amiloride-sensitive current at any potential between  $-140$  and  $+0$  mV (Figure 1B).

These results are in contrast to previous reports from oocytes expressing rat ENaC, which were insensitive to  $\text{Cd}^{2+}$  even at high concentration (Takeda et al. 2007). The differences in the response of xENaC and rENaC to extracellular  $\text{Cd}^{2+}$  may arise from the differences in their extracellular domain, as discussed later in the modeling studies.

The effect of  $\text{Cd}^{2+}$  is rapid and partially reversible, as shown in Figure 2A. However, the lack of complete reversibility might be masked by the rapid feedback inhibition characteristic for ENaC channel. Better and complete reversibility will be shown in experiments performed in A6 epithelial cells, in Figure 4. Figure 2B shows the dose-dependent inhibition of current at  $-60$  mV by  $\text{Cd}^{2+}$ . Relative currents

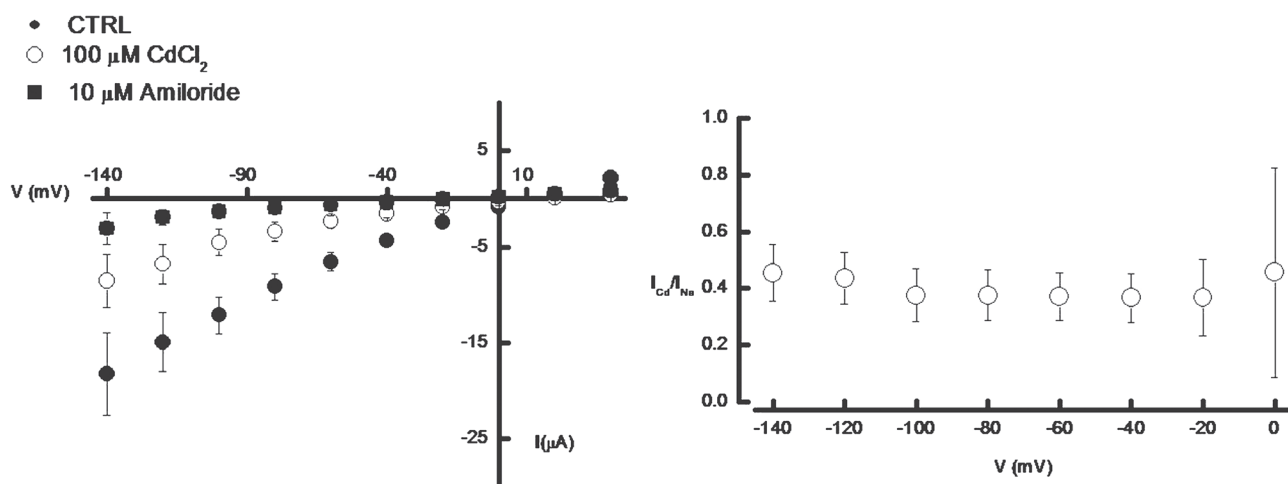


**Figure 1.** Inhibition of  $\alpha\beta\gamma$  xENaC by  $\text{Cd}^{2+}$ . **A.** Current-voltage (IV) relationship for oocytes expressing xENaC in the presence (●) or the absence (○) of  $100 \mu\text{M}$   $\text{Cd}^{2+}$  and with  $10 \mu\text{M}$  amiloride in the bath solution. The oocyte was held at 0 mV and tested from  $-140$  to  $+40$  mV in 20 mV increments for 500 ms at intervals of 1000 ms. **B.** Voltage-independent inhibition. Mean values of the normalized  $\text{Cd}^{2+}$ -inhibited currents plotted against membrane potential.

(IR) were obtained by normalizing the amiloride-sensitive currents in the presence of different Cd<sup>2+</sup> concentrations to the values under the control conditions. Data points are mean values  $\pm$  SEM for each concentration for  $n = 6$  oocytes. From these curves, the IC<sub>50</sub> was estimated as  $98 \pm 17 \mu\text{M}$  with a Hill coefficient  $n_H = 0.57 \pm 0.05$ . The experiments presented show that the inhibition was detectable at an agonist concentration of  $1 \mu\text{M}$  and reached the saturation level at  $2 \text{ mM}$ . We interpret a Hill coefficient value  $< 1$  as a negative cooperativity, in which the binding of Cd<sup>2+</sup> to one active site decreases the affinity of other sites.

#### Cd<sup>2+</sup> modulates ENaC from Na<sup>+</sup>-transporting epithelia

To confirm that the results obtained in oocytes expressing ENaC are reproducible in Na<sup>+</sup>-transporting epithelia, we

tested the effect of Cd<sup>2+</sup> in cells natively expressing the channel. A6 epithelial cells are considered a good model for studies of ENaC properties due to the high expression of  $\alpha\beta\gamma$  ENaC on the apical membrane. Moreover, the analysis of the effect of Cd<sup>2+</sup> on cells will provide more insights into the structural features of ENaC.

With  $100 \text{ mM}$  NaCl-containing solutions on the apical and the basolateral side of the monolayer, amiloride-sensitive currents of  $11.4 \pm 2.8 \mu\text{A}/\text{cm}^2$  were recorded ( $N = 5$  experiments). Similarly to oocytes expressing  $\alpha\beta\gamma$  *Xenopus* channel, ENaC-mediated currents were blocked by Cd<sup>2+</sup>. When the apical membrane of A6 epithelium was exposed to  $500 \mu\text{M}$  Cd<sup>2+</sup>, the short-circuit current ( $I_{sc}$ ) and transepithelial conductance ( $G_T$ ) were rapidly and reversibly inhibited by the metal (Fig. 3A). Fig. 3B summarizes the normalized amiloride-sensitive currents before, during and after expo-

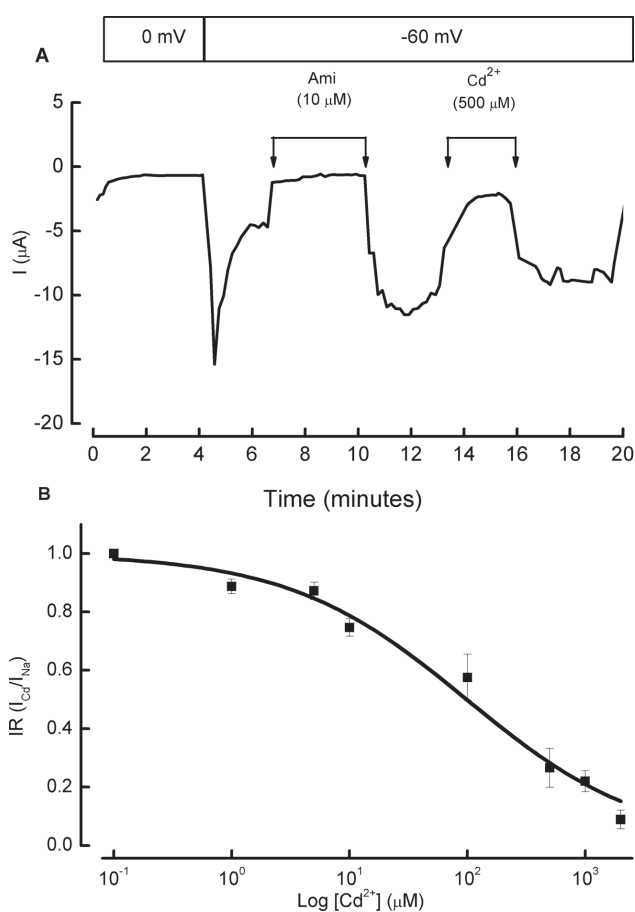


**Figure 2.** Effect of Cd<sup>2+</sup> inhibition at  $-60 \text{ mV}$  in xENaC expressing oocytes. **A.** Representative time-course experiment demonstrating inhibition of  $I_{\text{Na}}$  by  $500 \mu\text{M}$  Cd<sup>2+</sup> compared to the effect of  $10 \mu\text{M}$  amiloride (Ami). **B.** Dose-dependent curve of Cd<sup>2+</sup> inhibition. Each point represents averages  $\pm$  SEM of  $n = 6$  oocytes. Solid line represents the nonlinear fit of the data with the Hill equation, where  $\text{IC}_{50} = 98 \pm 17 \mu\text{M}$  with Hill coefficient  $n_H = 0.57 \pm 0.05$ .

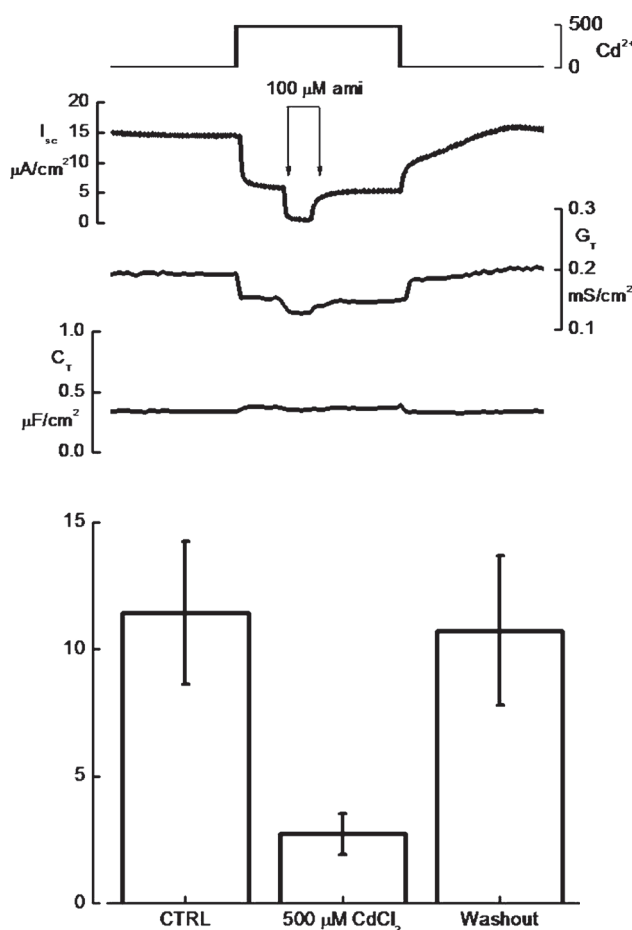


**Figure 3.** Representative example testing the effect of  $500 \mu\text{M}$  CdCl<sub>2</sub> on the apical membrane of A6 cells. **A.** Cd<sup>2+</sup> reduced the short circuit current ( $I_{sc}$ ) and the transepithelial conductance ( $G_T$ ) but had no effect on the transepithelial capacitance ( $C_T$ ). **B.** The addition of  $500 \mu\text{M}$  Cd<sup>2+</sup> inhibited amiloride Na<sup>+</sup> current, which was rapidly and completely recovered after Cd<sup>2+</sup> removal ( $N = 5$ ).

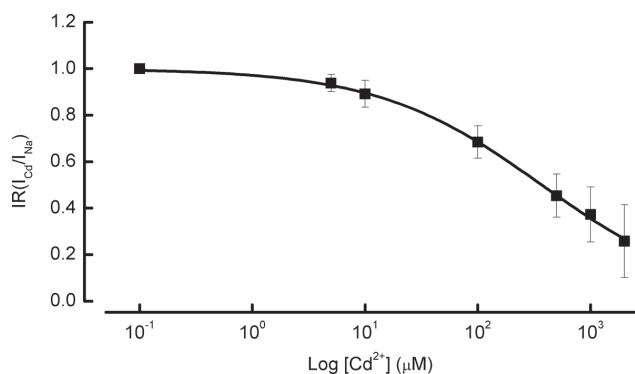


**Figure 4.** Dose-response curve of  $\text{Cd}^{2+}$  inhibition plotted as the normalized ENaC current in A6 cells in short-circuit conditions. Each point represents the mean  $\pm$  SEM of 8 experiments ( $N = 8$ ). Solid line represents the best fit by nonlinear regression to the Hill equation, see “Materials and Methods”.  $\text{IC}_{50} = 368 \pm 98.7 \mu\text{M}$  and  $n_H = 0.59 \pm 0.1$ .

sure to  $\text{Cd}^{2+}$ . After exposure to  $\text{Cd}^{2+}$ , the currents completely recovered in approximately 30 minutes.

In addition to short-circuit current and conductance, the system enables the concomitant estimation of capacitance. Membrane capacitance is proportional to the membrane area. Increases in capacitance point toward an increase in functional channels mediated by the insertion of channels into the apical membrane (Van Driessche and Erlj 1991; Alvarez de la Rosa et al. 2004). This method was successfully used to prove the exocytosis of new ENaC channels secondary to the treatment of the epithelium with cAMP or insulin (Erlj et al. 1994; Atia et al. 1999).

$\text{Cd}^{2+}$  had no significant effect on the transepithelial capacitance ( $C_T$ ) and in consequence on channels insertion in the apical membrane of A6 epithelia (Fig. 3A).

Similarly to ENaC-injected oocytes,  $\text{Cd}^{2+}$  dose-dependently inhibited ENaC currents (Fig. 4) in A6 epithelia. The inhibition of  $\text{Na}^+$  currents ( $I_{\text{Na}}$ ) was half-maximal ( $\text{IC}_{50}$ ) at  $368 \pm 98.7 \mu\text{M}$  and  $n_H = 0.59 \pm 0.1$  for  $N = 8$  experiments.

The reason that the Hill coefficient was  $\sim 0.6$  in both sets of experiments, oocytes and A6 cells, will have to be determined by further experiments. In this phase of the study, the results could be interpreted as a reflection of negative cooperativity, in which the binding of  $\text{Cd}^{2+}$  to one active site decreases the affinity of other sites for the ion (Yifrach 2004).

We further aimed to investigate whether  $\text{Cd}^{2+}$  interferes with amiloride binding in xENaC. Amiloride inhibited ENaC currents with half-maximal inhibition at a concentration of  $0.09 \pm 0.01 \mu\text{M}$  under control conditions ( $N = 5$ ). In the presence of  $500 \mu\text{M}$   $\text{Cd}^{2+}$ , in the apical bath, for the same cells, the effect of amiloride was significantly lower, with an  $\text{IC}_{50}$  of  $0.4 \pm 0.06 \mu\text{M}$  (Fig. 5). In both cases, the Hill

coefficients were near 1, which is consistent with a positive cooperativity for amiloride.

From these experiments, it is clear that  $\text{Cd}^{2+}$  perturbs amiloride binding, like other metal ions that interact with amiloride (Segal et al. 2002; Cucu et al. 2003). This effect might be caused by blocking its accessibility and inducing a conformational change of the binding site (allosteric competition) or by competing directly with amiloride for the same position (isosteric competition). To investigate these situations, we performed molecular simulations of ENaC.

#### Structural models of rENaC and xENaC

The homology modeling of rENaC and xENaC is supported by available crystal structures of ASIC1 and considers a) the conformational state, b) the most appropriate structure for the glycosylated extracellular loops, c) TM domains with the selectivity filter and d) the configuration of the channel pore.

The trimeric conformation of ENaC is based on the first solved crystal structure of ASIC1 (Jasti et al. 2007). This structure revealed that the channel assembles into a trimeric protein with two transmembrane domains *per* monomer and a multidomain extracellular loop enriched in acidic residues and carboxyl-carboxylate pairs. The extracellular loop of ASIC1 resembles a hand, and therefore components such as the wrist, palm, thumb, finger, and knuckle were used to denote specific domains (Jasti et al. 2007). Each of the wrist, palm, thumb and knuckle domains were found to exhibit good homology with ENaC (Jasti et al. 2007; Stockand et al. 2008; Kashlan et al. 2011; Kashlan and Kleyman 2011). In contrast, the finger domain showed a poor homology with the finger domain from the ASIC1 structure (Jasti et al. 2007; Stockand et al. 2008; Kashlan et al. 2011; Kashlan and Kleyman 2011). Using data derived from peptide binding to

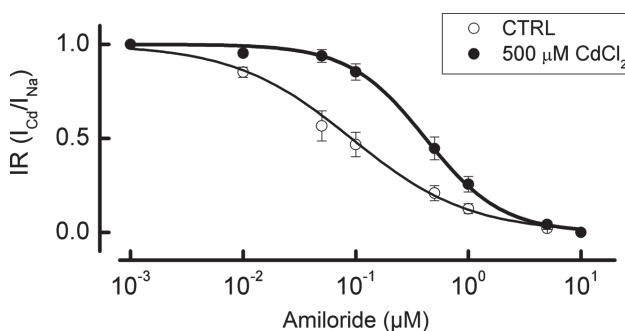


**Figure 5.** The amiloride affinity is changed by  $\text{Cd}^{2+}$ . Dose response curve for amiloride in the presence and absence of  $500 \mu\text{M}$   $\text{Cd}^{2+}$  for  $N = 5$  experiments. Using Hill equation,  $\text{IC}_{50}$  was  $0.09 \pm 0.008 \mu\text{M}$  in the absence of  $\text{Cd}^{2+}$  (○) and  $0.4 \pm 0.06 \mu\text{M}$  in the presence of the metal ion (●) and  $n_H = 1$ . CTRL, control.

the  $\alpha$  subunit of mouse ENaC, a previous study determined distance constraints that suggested the existence of a long  $\alpha 2$  helix in the finger domain (Kashlan et al. 2011). This template was used to build the extracellular loops of  $\alpha\beta\gamma$  r-

and xENaC. The resulting conformations of the rENaC and xENaC backbones are very similar (the root mean square deviation between them is 0.75 Å). Therefore, Fig. 6a and b show only the xENaC model.

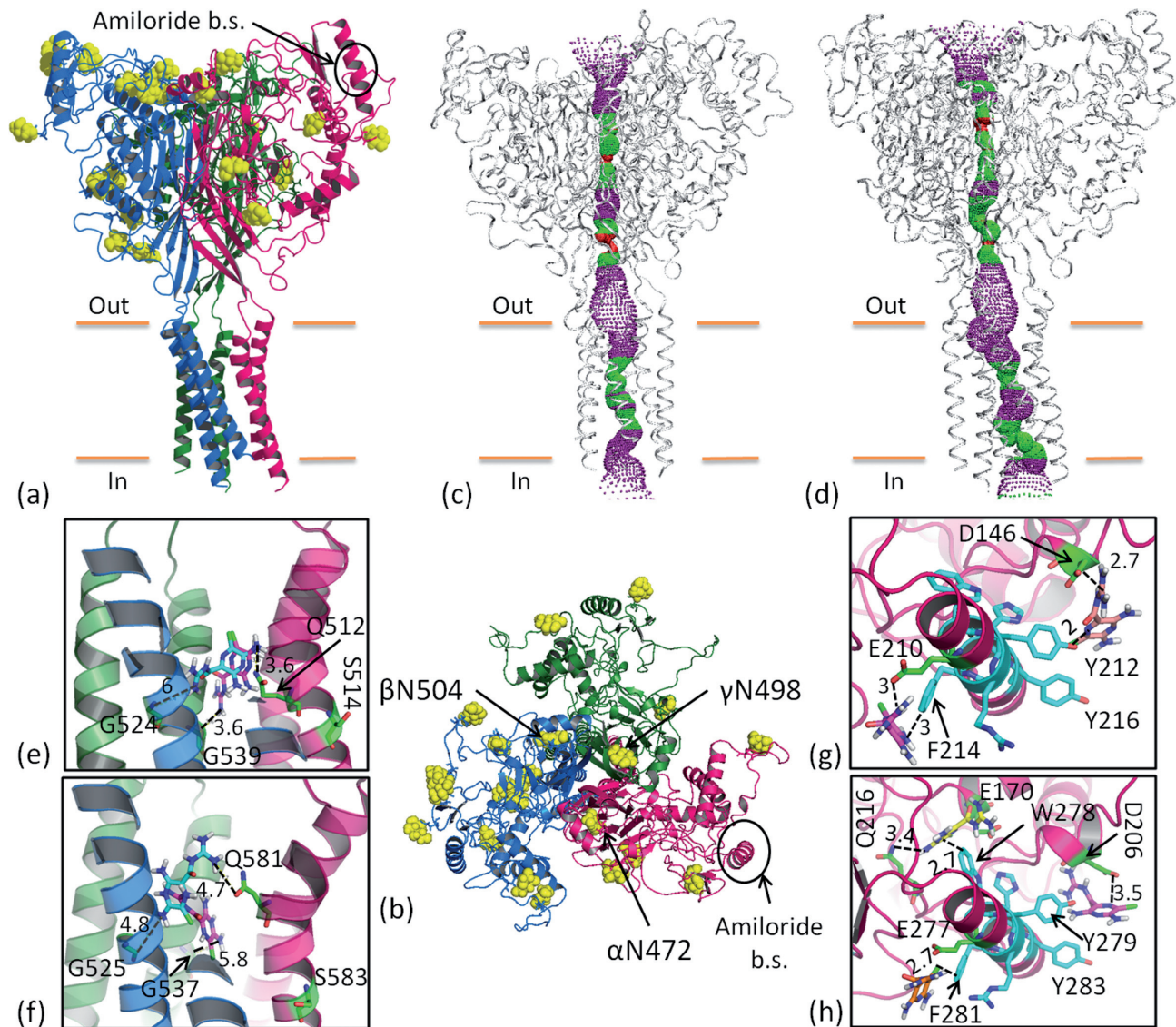


**Figure 6.** Side view (a) and top view (b) of the structural model of xENaC:  $\alpha$  subunit shown in pink,  $\beta$  in blue and  $\gamma$  in green. The extracellular amiloride binding site is marked in both (a) and (b). NAG residues attached to the channel are represented by yellow van der Waals spheres. In (b), the glycosylated ASN residues near the opening of the channel pore are labeled. The solvent-accessible pathways through xENaC and rENaC are presented in (c) and (d). Regions where the pore radius is less than 1.4 Å are displayed in red, regions with a pore radius between 1.4 Å and 2.5 Å are illustrated in green, and regions with a pore radius larger than 2.5 Å are shown in purple. The narrowest regions are located in the extracellular loops, whereas the TM pore is open with a radius larger than 1.4 Å. Docked amiloride molecules in the TM region of xENaC are shown in (e) and from rENaC in (f). Amiloride molecules are represented as blue and pink sticks. Channel subunits are colored as in (a) and (b). The amino acids involved in docking amiloride are represented as green sticks and labeled. The distances between these residues and amiloride molecules are also labeled. Docked amiloride molecules in the extracellular region of xENaC are shown in (g) and of rENaC in (h). Amiloride molecules are represented as pink, orange and yellow sticks. The residues that form the extracellular binding sites (the conserved sequence WYRFHY) are represented as blue sticks. Neighboring amino acids involved in the interaction with amiloride are represented as green sticks. Residues that interact with amiloride and the distances between them and amiloride are labeled.

Previous studies have shown that both ASIC1 and ENaC are glycosylated *in vivo* (Canessa et al. 1994; Snyder et al. 1994). Several ASIC1 crystal structures (PDB IDs: 2QTS, 3S3W, 3S3X, 4FZ0, 4FZ1, 4NTW) are glycosylated with a single NAG residue *per* glycosylation site (two in each subunit). Therefore, in this study, we focused on the experimentally identified rENaC glycosylation sites and on the following predicted sites: 10 sites in  $\beta$  rENaC, 5 sites in  $\gamma$  rENaC, 5 sites in  $\alpha$  xENaC, 12 sites in  $\beta$  xENaC and 4 sites in  $\gamma$  xENaC (Consortium, The UniProt, 2012). All these residues face the extracellular medium. The glycosylation sites are scattered throughout the extracellular loops of rENaC and xENaC (represented with yellow in Fig. 6b). In both models, three NAG residues (attached to  $\alpha$ N538,  $\beta$ N482 and  $\gamma$ N498 in rENaC and to  $\alpha$ N472,  $\beta$ N504 and  $\gamma$ N498 in xENaC) are located very close to the opening of the channel pore.

The molecular model of TM domains is also based on the crystal structures of ASIC. Currently, there are ten crystal structures of ASIC1 deposited in the Protein Data Bank: 2QTS (Jasti et al. 2007), 3IJ4, 4NYK (superseded 3HGC) (Gonzales et al. 2009), 3S3W, 3S3X (Dawson et al. 2012), 4FZ0, 4FZ1 (Bacongus and Gouaux 2012) and 4NTW, 4NTX, 4NTY (Bacongus et al. 2014). The structure 4FZ0 represents chicken ASIC1 crystallized at pH 5.5 and arrested in an open conformation upon binding to the spider toxin psalmotoxin. The crystal structure 4NTW represents the complex between ASIC and the snake toxin MitTx (Bacongus et al. 2014). Both the 4FZ0 and 4NTW structures possess Na<sup>+</sup>- and Li<sup>+</sup>-selective TM pores (Bacongus and Gouaux 2012; Bacongus et al. 2014). However, major differences are revealed between the architecture of the TM residues in the 4FZ0 and 4NTW structures. In the 4FZ0 structure, the TM residues form continuous  $\alpha$ -helices. In contrast, the second TM helix of the  $\alpha$  subunit from the 4NTW structure is discontinuous, switching its cytoplasmic one-third with an adjacent subunit (Bacongus et al. 2014). Moreover, as a large molecule, MitTx protrudes into the extracellular loop region at the interface between adjacent subunits. Additionally, the toxin forms strong contacts with the channel wrist, thumb and knuckle domains (Bacongus et al. 2014). In contrast, psalmotoxin is a small toxin binding in the cysteine-rich region of the extracellular domain with minimal perturbation of the protein backbone (Dawson et al. 2012). Therefore, the TM region of ASIC1 from the 4FZ0 structure was chosen as a template for modeling the TM region of ENaC.

The channel pores of the rENaC and xENaC models are asymmetric, with three wide vestibules separated by narrower regions. In Fig. 6c and d, the wide vestibules are represented in purple (pore radius > 2.5 Å), whereas the narrowest regions (pore radius < 1.4 Å) are represented in red. The narrowest regions are in the extracellular domains

of ENaC models. The pore in the TM regions is larger than 1.4 Å.

In the TM regions, the channel pore is lined by residues from both TM helices of each subunit. The first TM helix of the  $\gamma$  subunit contributes to the lining of the extracellular ENaC vestibule and is not involved in pore formation. The constrictions are produced by the hydrophobic and large side chains of Leu, Trp and Phe residues that protrude inside the pore and render a sinuous pore shape. This structure confirms the results of previous systematic mutagenesis studies that have shown the importance of aromatic amino acids in the vicinity of the selectivity filter (Kellenberger et al. 1999; Sheng et al. 2000) for the discrimination between Li<sup>+</sup> and Na<sup>+</sup> ions.

The TM channel pores open into the extracellular vestibules with a maximum radius of ~5.3 and ~6 Å for rENaC and xENaC, respectively. The extracellular vestibules communicate with the extracellular medium through three fenestrations that could allow ions to enter directly into the TM pore. Ion may also enter the channel pore through the upper vestibule. To understand how ions can access the TM pore, we calculated the distribution of potential energy on the ENaC model surfaces. As shown in Fig. 7, the surface of the channels' upper vestibules has a positive electrostatic potential as a result of the positively charged and polar residues that line the vestibules, such as  $\alpha$ R476,  $\alpha$ N477,  $\beta$ R509,  $\beta$ N510,  $\gamma$ K501 and  $\gamma$ K473 for xENaC and  $\alpha$ R545,  $\alpha$ N546,  $\beta$ R487,  $\beta$ K488,  $\gamma$ K496 and  $\gamma$ K499 for rENaC. The fenestrations are lined by regions from the wrist, the  $\beta$ 1 and  $\beta$ 12 sheets of the palm domains, and the lowest loops of the thumb domain. Their surfaces have a negative electrostatic potential, especially in the  $\beta$  and  $\gamma$  subunits of xENaC and in the  $\alpha$  and  $\beta$  subunits of rENaC. These regions include many negatively charged and polar amino acids whose side chains are exposed at the surface. This electrostatic distribution suggests that ions will enter the channel pore through these fenestrations.

In this pore configuration, the selectivity filters of both ENaC models (Palmer et al. 1990) are solvent accessible. The localizations of the selectivity filters and of the hydrophobic amino acid side chains inside the TM regions of the xENaC and rENaC pores are illustrated in Supplementary Fig. S2.

#### *Amiloride binding*

Previous studies have identified two amiloride binding sites. One of them, located close to the selectivity filter of ENaC, involves residues from all three subunits:  $\alpha$ S583,  $\beta$ G525 and  $\gamma$ G537 in rENaC (Kellenberger et al. 2003) and  $\alpha$ S514,  $\beta$ G547 and  $\gamma$ G539 in xENaC. This site interacts with the guanidinium group of amiloride, and the inhibition is voltage-dependent (Kellenberger et al. 2003). The other site, located in the extracellular loop of the  $\alpha$  ENaC subunit, is

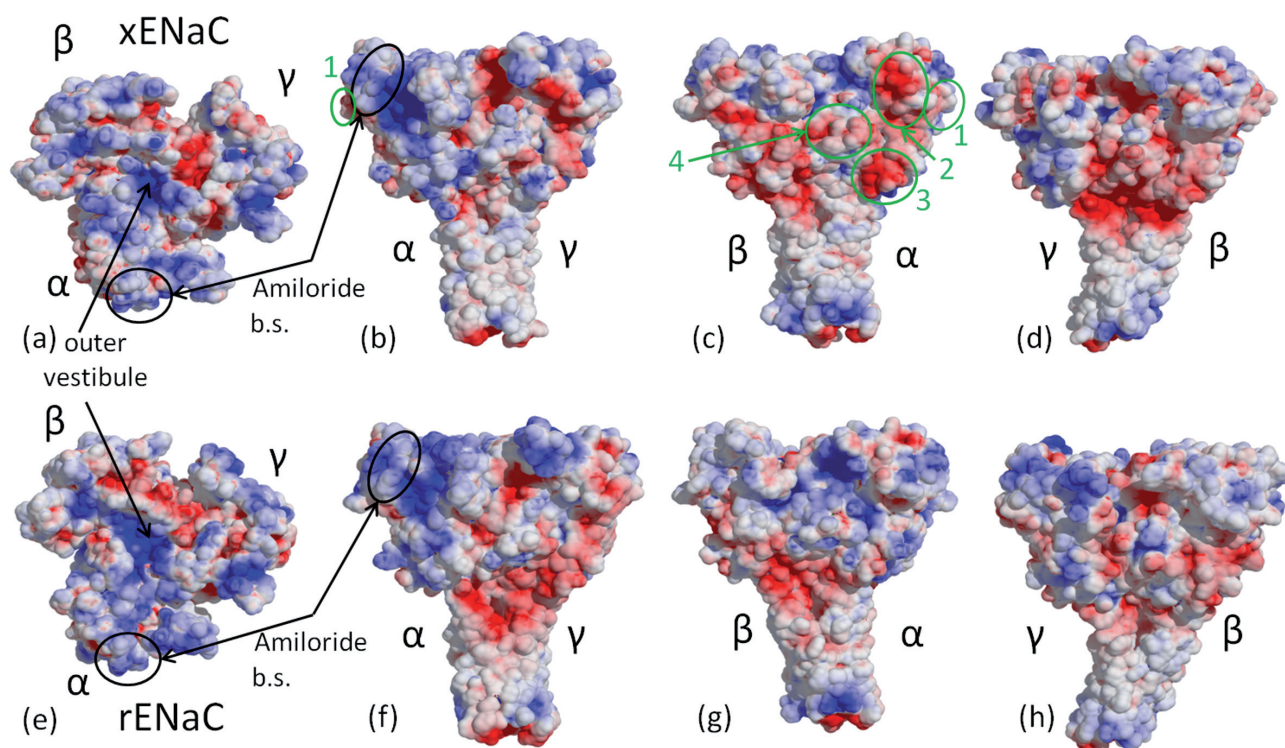


**Figure 7.** Distribution of the electrostatic potential on the surface of xENaC (top view (a), side views (b, c and d) and rENaC (top view (e), side views (f, g and h)). Regions with negative electrostatic potential ( $< -5$  kT/e) are represented in red and regions with positive electrostatic potential ( $> 5$  kT/e) in blue. The side views of ENaC models were obtained by rotating the channel so that all subunits are visible (labeled on the figure). The extracellular amiloride binding site is circled with black, and the putative Cd<sup>2+</sup> binding sites are circled with green and are numbered according to the distance between them and the amiloride binding site, where 1 is the closest.

represented by the WYRFHY sequence (residues 278-283 in  $\alpha$  rENaC and residues 211-216 in  $\alpha$  xENaC) and interacts with the pyrazine ring of the amiloride molecule (Kelly et al. 2003).

The ability of the rENaC and xENaC models to bind amiloride was investigated by docking amiloride to both these binding sites. In these ENaC models, the amiloride binding sites found near the selectivity filters are located in the middle of the lipid bilayer. Most of the residues identified as participating in the binding of amiloride are solvent accessible. The exceptions are the residues  $\alpha$ S583 and  $\alpha$ S514 from rENaC and xENaC, respectively, which face away from the channel pore. The amiloride molecule is protonated, and the surface of the channel pore in the TM region has a negative electrostatic potential. Therefore, amiloride can bind in several orientations at different depths in the channel pore. However, for each model, we found only two possible orientations of amiloride that can dock close to the putative amiloride binding sites from the  $\beta$  and  $\gamma$  subunits (see Fig. 6e and f). In the xENaC pore, the amiloride guanidinium group is involved in the interaction with the amiloride binding site, whereas the pyrazine ring interacts with  $\alpha$ Q512. For

rENaC, the interaction with the binding site is mediated by the pyrazine ring of amiloride, and the guanidinium group interacts with  $\alpha$ Q581.

In both models, the residues that form the extracellular binding sites are located on the  $\alpha$ 2 helix (see Fig. 6g and h). For  $\alpha$  xENaC, the best docked amiloride molecules cluster in two locations. Therefore, Fig. 6g shows two representative structures, one from each cluster. As illustrated, the pyrazine ring of amiloride interacts with  $\alpha$ Y212 or with  $\alpha$ F214. In both configurations, the guanidinium group of amiloride interacts with negatively charged residues that are spatially close to the amiloride molecules:  $\alpha$ D146 or  $\alpha$ E210. Similarly to xENaC, in the case of rENaC, we observed the same tendency of docked amiloride molecules to cluster. We identified three clusters, in which the pyrazine ring of amiloride interacts with  $\alpha$ W278,  $\alpha$ Y279 or  $\alpha$ F281, whereas the guanidinium groups interact with  $\alpha$ Q216,  $\alpha$ E170,  $\alpha$ D206 or  $\alpha$ E277. Three representative structures from each cluster are presented in 6h.

Both ENaC and ASIC1 are inhibited by amiloride. Therefore, we compared the locations of the docked amiloride conformations identified here with the locations of amiloride

molecules bound to the chicken ASIC1-MitTx complex, as determined by Bacongus et al. (2014) using ASIC1-MitTx crystals soaked in amiloride solution (PDB code: 4NTX). Amiloride molecules bound to ASIC1 are located in the acidic pocket and in the extracellular vestibule. In the ENaC models that we built, the acidic pockets are almost occluded by the  $\alpha 1$  helices formed by residues with no homology to the ASIC1 structure (see Supplementary Fig. S1), and therefore, amiloride cannot bind at these sites. In the extracellular vestibules of the ENaC models, amiloride molecules can be docked in several orientations, including the extracellular vestibule. This conformation is similar to the orientation of amiloride in ASIC1.

#### Putative $\text{Cd}^{2+}$ binding sites

Considering that  $\text{Cd}^{2+}$  inhibits only xENaC in a voltage-independent manner, we assume that it may bind on the xENaC surface in markedly electronegative regions with little or no correspondence to the extracellular surface of rENaC. Therefore, to identify the putative  $\text{Cd}^{2+}$  binding sites in xENaC, we compared the surface electrostatic potential distributions of xENaC and rENaC. As shown in Fig. 7, relative to rENaC, the surface of xENaC has wider electronegative regions, particularly on the  $\alpha$  subunit. These differences are not surprising, given that the  $\alpha$  rENaC and  $\alpha$  xENaC subunits share only 58% identity and 73% homology. Based on the competition between  $\text{Cd}^{2+}$  and amiloride binding, as shown in Fig. 4, and because the extracellular binding site of amiloride is found in the  $\alpha$  subunit, we assume that the  $\text{Cd}^{2+}$  binding site is located in the extracellular loop of the  $\alpha$  rENaC subunit.

The surfaces with the desired properties are highlighted in green in Fig. 7 and numbered according to their proximity to amiloride binding site. The closest putative  $\text{Cd}^{2+}$  binding site (CD1) is formed by the residues  $\alpha\text{E191}$ ,  $\alpha\text{T192}$  and  $\alpha\text{Q225}$  and is found 6 Å from  $\alpha\text{F214}$ , which is identified as participating in amiloride binding. The second closest  $\text{Cd}^{2+}$  binding site (CD2) is found ~16 Å from  $\alpha\text{F214}$  and is formed by the  $\alpha\text{E172}$ ,  $\alpha\text{E173}$ ,  $\alpha\text{E174}$  and  $\alpha\text{D195}$  residues. Two putative binding sites are located at a great distance from the amiloride binding site: ~40 Å in the case of the third binding site (CD3) and ~50 Å in the case of the fourth (CD4). CD3 is formed by residues from the thumb domain:  $\alpha\text{E357}$ ,  $\alpha\text{D358}$ ,  $\alpha\text{S360}$ ,  $\alpha\text{S370}$  and  $\alpha\text{E371}$ . They are located on the loop that connects the  $\beta 9$  sheet from the palm domain with the  $\alpha 4$  helix from the thumb. The residues in CD4,  $\alpha\text{N244}$ ,  $\alpha\text{E245}$  and  $\alpha\text{E246}$  are located in the palm domain and are part of the loop that connects the  $\beta 3$  sheet from the palm domain with the  $\beta 4$  sheet from the  $\beta$ -ball domain. The localizations of  $\text{Cd}^{2+}$  binding sites are presented in Fig. S3. The work of Bacongus et al. (2014) determined the structure of ASIC1

in ASIC1-MitTx crystals soaked in CsCl solution (PDB code: 4NTY). We compared the location of the 15  $\text{Cs}^+$  ions within the 4NTY structure with the locations of the putative  $\text{Cd}^{2+}$  binding sites from a xENaC. Using this approach, residues spatially aligned with the corresponding predicted binding site for  $\text{Cd}^{2+}$ , designated as CD3, were identified. The residues from this binding site present good homology with ASIC1.

From the ENaC structure, one might assume that  $\text{Cd}^{2+}$  also binds in the selectivity filter of the channel or in the rich cysteine domain for the extracellular loops. Because these sequences are highly conserved, and the effect of  $\text{Cd}^{2+}$  is different in rENaC compared to xENaC, other domains should be taken into consideration.

Normal mode analysis, performed on chicken ASIC1 by Yang et al. (2009), revealed that channel gating is correlated by collective motions of the thumb and finger domains, facilitated by attractive forces between these domains. The results were confirmed by site-directed mutagenesis experiments (Yang et al. 2009). Three of the possible  $\text{Cd}^{2+}$  binding sites were identified in the  $\alpha$  xENaC structure and are denoted as CD1, CD2 and CD3. These sites are located in the finger and thumb domains (see Fig. S3). CD1 is positioned close to the interface between the thumb and finger domains. In light of the results from Yang et al. (2009), we assume that  $\text{Cd}^{2+}$  binding to these sites and especially to CD1 might perturb the finger and thumb domains flexibility. Moreover,  $\text{Cd}^{2+}$  binding to CD1, which is close to the amiloride binding site, might also perturb amiloride binding. These results are consistent with the experimental data presented in Fig. 3.

#### Conclusions

The results from cells heterologously expressing ENaC and from  $\text{Na}^+$ -transporting epithelia indicate that ENaC is inhibited by extracellular  $\text{Cd}^{2+}$ . As the concentration of  $\text{Cd}^{2+}$  increased, a dose-dependent reduction in  $\text{Na}^+$  current was obtained in both cellular models. Because  $\text{Cd}^{2+}$  addition and removal alter the ENaC current over a rapid time course, it seems likely that  $\text{Cd}^{2+}$  affects channel activity rather than changing ENaC trafficking. This presumption is sustained by the results obtained from measurements on epithelial A6 cells, in which no changes in transepithelial capacitance were observed upon  $\text{Cd}^{2+}$  addition.

The inhibition of ENaC by  $\text{Cd}^{2+}$  has much in common with the effect of  $\text{Cd}^{2+}$  on acid-sensing ion channels (Staruschenko et al. 2007), being rapid and voltage-independent. However, these data contrast with the results obtained using mouse-ENaC, which was insensitive to extracellular  $\text{Cd}^{2+}$ , whereas rat-ENaC was insensitive to external  $\text{Cd}^{2+}$  but blocked by cytosolic  $\text{Cd}^{2+}$  (Kellenberger et al. 2005).

In Na<sup>+</sup>-transporting epithelia, a clear diminution of amiloride affinity was obtained in the presence of Cd<sup>2+</sup>, which indicates a competition between two compounds for the same binding site. A better explanation would be that Cd<sup>2+</sup> changes the conformation of ENaC so that amiloride cannot reach its site located in the channel pore. To offer new insights into this hypothesis, we performed molecular modeling. We show that the xENaC structure presents four putative binding sites for Cd<sup>2+</sup> based on the sum of the experimental data: 1) vicinity of the amiloride binding site; 2) no correspondence with sites in rENaC that are Cd<sup>2+</sup>-insensitive; and 3) marked electronegativity potential sustaining the voltage-independent binding manner. In this phase of the study, we lack information about the effect of Cd<sup>2+</sup> on human ENaC, which would offer more insights regarding the toxicology of this hazardous metal. However, the effects on reptilian or mammalian membrane transport should not be minimized. Moreover, this report provides information about the structure and modeling of ENaC. Furthermore, we are considering a continuation this study through mutagenesis analysis on ENaC.

These results and others that show the sensitivity of ENaC to heavy metals (Yu et al. 2007), protons (Collier and Snyder 2009), and temperature variation (Chraibi and Horisberger 2002), qualify ENaC as a sensor for environmental signals.

**Acknowledgements.** We thank Dr. Eugen Gheorghiu and Dr. Nina D. Ullrich for their helpful comments on the manuscript. We thank Dr. Norica Branza-Nichita and Catalin Lazar for their help with cRNA synthesis and Professor Willy Van Driessche for the assistance provided during the installation of electrophysiology setups in our laboratory. We are grateful to Dr. J. D. Horisberger and Dr. B. Rossier for making available the cDNA of xENaC. This work was supported by the National Authority of Research with the program Nr. 41-013/18.09.2007 and by the Romanian Ministry of Education, Research, Youth and Sport through the "IDEAS" project 137/2011.

## References

- Alvarez de la Rosa D., Paunescu T. G., Els W. J., Helman S. I., Canessa C. M. (2004): Mechanisms of regulation of epithelial sodium channel by SGK1 in A6 cells. *J. Gen. Physiol.* **124**, 395–407  
<http://dx.doi.org/10.1085/jgp.200409120>
- Amuzescu B., Segal A., Flonta M. L., Simaels J., Van Driessche W. (2003): Zinc is a voltage-dependent blocker of native and heterologously expressed epithelial Na<sup>+</sup> channels. *Pflügers. Arch.* **446**, 69–77  
<http://dx.doi.org/10.1007/s00424-002-0998-3>
- Atia F., Zeiske W., van Driessche W. (1999): Secretory apical Cl<sup>-</sup> channels in A6 cells: possible control by cell Ca<sup>2+</sup> and cAMP. *Pflügers. Arch.* **438**, 344–353  
<http://dx.doi.org/10.1007/s004240050919>
- Awayda M. S., Ismailov I. I., Berdiev B. K., Fuller C. M., Benos D. J. (1996): Protein kinase regulation of a cloned epithelial Na<sup>+</sup> channel. *J. Gen. Physiol.* **108**, 49–65  
<http://dx.doi.org/10.1085/jgp.108.1.49>
- Baconguis I., Bohlen C. J., Goehring A., Julius D., Gouaux E. (2014): X-ray structure of Acid-sensing ion channel 1-snake toxin complex reveals open state of a Na<sup>+</sup>-selective channel. *Cell* **156**, 717–729  
<http://dx.doi.org/10.1016/j.cell.2014.01.011>
- Baconguis I., Gouaux E. (2012): Structural plasticity and dynamic selectivity of acid-sensing ion channel-spider toxin complexes. *Nature* **489**, 400–405  
<http://dx.doi.org/10.1038/nature11375>
- Baker N. A., Sept D., Joseph S., Holst M. J., McCammon J. A. (2001): Electrostatics of nanosystems: application to microtubules and the ribosome. *Proc. Natl. Acad. Sci. U.S.A.* **98**, 10037–10041  
<http://dx.doi.org/10.1073/pnas.181342398>
- Barbier O., Jacquillet G., Tauc M., Poujeol P., Cougnon M. (2004): Acute study of interaction among cadmium, calcium, and zinc transport along the rat nephron in vivo. *Am. J. Physiol. Renal Physiol.* **287**, F1067–1075  
<http://dx.doi.org/10.1152/ajprenal.00120.2004>
- Bathula C. S., Garrett S. H., Zhou X. D., Sens M. A., Sens D. A., Somji S. (2008): Cadmium, vectorial active transport, and MT-3-dependent regulation of cadherin expression in human proximal tubular cells. *Toxicol. Sci.* **102**, 310–318  
<http://dx.doi.org/10.1093/toxsci/kfn004>
- Best R. B., Zhu X., Shim J., Lopes P. E. M., Mittal J., Feig M., MacKerell A. D. (2012): Optimization of the additive CHARMM all-atom protein force field targeting improved sampling of the backbone  $\phi$ ,  $\psi$  and side-chain  $\chi_1$  and  $\chi_2$  dihedral angles. *J. Chem. Theory Comput.* **8**, 3257–3273  
<http://dx.doi.org/10.1021/ct300400x>
- Boveri M., Pazos P., Gennari A., Casado J., Hartung T., Prieto P. (2004): Comparison of the sensitivity of different toxicological endpoints in Caco-2 cells after cadmium chloride treatment. *Arch. Toxicol.* **78**, 201–206  
<http://dx.doi.org/10.1007/s00204-003-0532-1>
- Brooks B. R., Brooks C. L., 3rd, Mackerell A. D., Jr., Nilsson L., Petrella R. J., Roux B., Won Y., Archontis G., Bartels C., Boresch S. et al. (2009): CHARMM: the biomolecular simulation program. *J. Comput. Chem.* **30**, 1545–1614  
<http://dx.doi.org/10.1002/jcc.21287>
- Canessa C. M., Merillat A. M., Rossier B. C. (1994): Membrane topology of the epithelial sodium channel in intact cells. *Am. J. Physiol.* **267**, C1682–1690
- Chraibi A., Horisberger J. D. (2002): Na self inhibition of human epithelial Na channel: temperature dependence and effect of extracellular proteases. *J. Gen. Physiol.* **120**, 133–145  
<http://dx.doi.org/10.1085/jgp.20028612>
- Collier D. M., Snyder P. M. (2009): Extracellular protons regulate human ENaC by modulating Na<sup>+</sup> self-inhibition. *J. Biol. Chem.* **284**, 792–798  
<http://dx.doi.org/10.1074/jbc.M806954200>
- Consortium T. U. (2012): Reorganizing the protein space at the Universal Protein Resource (UniProt). *Nucleic Acids Res.* **40**, D71–75

- <http://dx.doi.org/10.1093/nar/gkr981>
- Cucu D., D'Haese P. C., De Beuf A., Verhulst A. (2011): Low doses of cadmium chloride and methallothionein-1-bound cadmium display different accumulation kinetics and induce different genes in cells of the human nephron. *Nephron extra* **1**, 24–37  
<http://dx.doi.org/10.1159/000330069>
- Cucu D., Simaels J., Eggermont J., Van Driessche W., Zeiske W. (2005): Opposite effects of Ni<sup>2+</sup> on *Xenopus* and rat ENaCs expressed in *Xenopus* oocytes. *Am. J. Physiol. Cell Physiol.* **289**, C946–958  
<http://dx.doi.org/10.1152/ajpcell.00419.2004>
- Dawson R. J., Benz J., Stohler P., Tetaz T., Joseph C., Huber S., Schmid G., Hugin D., Pflimlin P., Trube G. et al. (2012): Structure of the acid-sensing ion channel 1 in complex with the gating modifier Psalmotoxin 1. *Nat. Commun.* **3**, 936  
<http://dx.doi.org/10.1038/ncomms1917>
- Erlj D., De Smet P., Van Driessche W. (1994): Effect of insulin on area and Na<sup>+</sup> channel density of apical membrane of cultured toad kidney cells. *J Physiol.* **481**, 533–542  
<http://dx.doi.org/10.1113/jphysiol.1994.sp020461>
- Eswar N., Webb B., Marti-Renom M. A., Madhusudhan M. S., Eramian D., Shen M. Y., Pieper U., Sali A. (2007): Comparative protein structure modeling using MODELLER. *Curr. Protoc. Protein Sci.* **2**, 2.9
- Gonzales E. B., Kawate T., Gouaux E. (2009): Pore architecture and ion sites in acid-sensing ion channels and P2X receptors. *Nature* **460**, 599–604  
<http://dx.doi.org/10.1038/nature08218>
- Guvench O., Greene S. N., Kamath G., Brady J. W., Venable R. M., Pastor R. W., Mackerell A. D., Jr. (2008): Additive empirical force field for hexopyranose monosaccharides. *J. Comput. Chem* **29**, 2543–2564  
<http://dx.doi.org/10.1002/jcc.21004>
- Jasti J., Furukawa H., Gonzales E. B., Gouaux E. (2007): Structure of acid-sensing ion channel 1 at 1.9 Å resolution and low pH. *Nature* **449**, 316–323  
<http://dx.doi.org/10.1038/nature06163>
- Kashlan O. B., Adelman J. L., Okumura S., Blobner B. M., Zuzek Z., Hughey R. P., Kleyman T. R., Grabe M. (2011): Constraint-based, homology model of the extracellular domain of the epithelial Na<sup>+</sup> channel alpha subunit reveals a mechanism of channel activation by proteases. *J. Biol. Chem.* **286**, 649–660  
<http://dx.doi.org/10.1074/jbc.M110.167098>
- Kashlan O. B., Kleyman T. R. (2011): ENaC structure and function in the wake of a resolved structure of a family member. *Am. J. Physiol. Renal Physiol.* **301**, F684–696  
<http://dx.doi.org/10.1152/ajprenal.00259.2011>
- Kellenberger S., Gautschi I., Pfister Y., Schild L. (2005): Intracellular thiol-mediated modulation of epithelial sodium channel activity. *J. Biol. Chem.* **280**, 7739–7747  
<http://dx.doi.org/10.1074/jbc.M409955200>
- Kellenberger S., Gautschi I., Schild L. (2003): Mutations in the epithelial Na<sup>+</sup> channel ENaC outer pore disrupt amiloride block by increasing its dissociation rate. *Mol. Pharmacol.* **64**, 848–856  
<http://dx.doi.org/10.1124/mol.64.4.848>
- Kellenberger S., Hoffmann-Pochon N., Gautschi I., Schneeberger E., Schild L. (1999): On the molecular basis of ion permeation in the epithelial Na<sup>+</sup> channel. *J. Gen. Physiol.* **114**, 13–30  
<http://dx.doi.org/10.1085/jgp.114.1.13>
- Kelly O., Lin C., Ramkumar M., Saxena N. C., Kleyman T. R., Eaton D. C. (2003): Characterization of an amiloride binding region in the alpha-subunit of ENaC. *Am. J. Physiol. Renal Physiol.* **285**, F1279–1290  
<http://dx.doi.org/10.1152/ajprenal.00094.2003>
- Larkin M. A., Blackshields G., Brown N. P., Chenna R., McGettigan P. A., McWilliam H., Valentin F., Wallace I. M., Wilm A., Lopez R. et al. (2007): Clustal W and Clustal X version 2.0. *Bioinformatics* **23**, 2947–2948  
<http://dx.doi.org/10.1093/bioinformatics/btm404>
- Li H., Robertson A. D., Jensen J. H. (2005): Very fast empirical prediction and rationalization of protein pKa values. *Proteins* **61**, 704–721  
<http://dx.doi.org/10.1002/prot.20660>
- MacKerell A. D., Bashford D., Bellott M., Dunbrack R. L., Evanseck J. D., Field M. J., Fischer S., Gao J., Guo H., Ha S. et al. (1998): All-atom empirical potential for molecular modeling and dynamics studies of proteins. *J. Phys. Chem. B* **102**, 3586–3616  
<http://dx.doi.org/10.1021/jp973084f>
- MacKerell A. D., Feig M., Brooks C. L. (2003): Improved treatment of the protein backbone in empirical force fields. *J. Am. Chem. Soc.* **126**, 698–699  
<http://dx.doi.org/10.1021/ja036959e>
- Markovich D., Knight D. (1998): Renal Na-Si cotransporter NaSi-1 is inhibited by heavy metals. *Am. J. Physiol.* **274**, F283–289
- Nordberg G. F., Jin T., Wu X., Lu J., Chen L., Lei L., Hong F., Nordberg M. (2009): Prevalence of kidney dysfunction in humans-relationship to cadmium dose, metallothionein, immunological and metabolic factors. *Biochimie* **91**, 1282–1285  
<http://dx.doi.org/10.1016/j.biochi.2009.06.014>
- Nutter-Upham K. E., Saykin A. J., Rabin L. A., Roth R. M., Wishart H. A., Pare N., Flashman L. A. (2008): Verbal fluency performance in amnesic MCI and older adults with cognitive complaints. *Arch. Clin. Neuropsychol.* **23**, 229–241  
<http://dx.doi.org/10.1016/j.acn.2008.01.005>
- Palmer L. G., Corthesy-Theulaz I., Gaeggeler H. P., Kraehenbuhl J. P., Rossier B. (1990): Expression of epithelial Na channels in *Xenopus* oocytes. *J. Gen. Physiol.* **96**, 23–46  
<http://dx.doi.org/10.1085/jgp.96.1.23>
- Park K., Kim K. R., Kim J. Y., Park Y. S. (1997): Effect of cadmium on Na-Pi cotransport kinetics in rabbit renal brush-border membrane vesicles. *Toxicol. Appl. Pharmacol.* **145**, 255–259  
<http://dx.doi.org/10.1006/taap.1997.8180>
- Sheng S., Li J., McNulty K. A., Avery D., Kleyman T. R. (2000): Characterization of the selectivity filter of the epithelial sodium channel. *J. Biol. Chem.* **275**, 8572–8581  
<http://dx.doi.org/10.1074/jbc.275.12.8572>
- Sheng S., Perry C. J., Kleyman T. R. (2002): External nickel inhibits epithelial sodium channel by binding to histidine residues within the extracellular domains of alpha and gamma subunits and reducing channel open probability. *J. Biol. Chem.* **277**, 50098–50111  
<http://dx.doi.org/10.1074/jbc.M209975200>
- Sheng S., Perry C. J., Kleyman T. R. (2004): Extracellular Zn<sup>2+</sup> activates epithelial Na<sup>+</sup> channels by eliminating Na<sup>+</sup> self-inhibition. *J. Biol. Chem.* **279**, 31687–31696  
<http://dx.doi.org/10.1074/jbc.M405224200>

- Smart O. S., Goodfellow J. M., Wallace B. A. (1993): The pore dimensions of gramicidin A. *Biophys. J.* **65**, 2455–2460  
[http://dx.doi.org/10.1016/S0006-3495\(93\)81293-1](http://dx.doi.org/10.1016/S0006-3495(93)81293-1)
- Snyder P. M., McDonald F. J., Stokes J. B., Welsh M. J. (1994): Membrane topology of the amiloride-sensitive epithelial sodium channel. *J. Biol. Chem.* **269**, 24379–24383
- Staruschenko A., Dorofeeva N. A., Bolshakov K. V., Stockand J. D. (2007): Subunit-dependent cadmium and nickel inhibition of acid-sensing ion channels. *Dev. Neurobiol.* **67**, 97–107  
<http://dx.doi.org/10.1002/neu.20338>
- Stockand J. D., Staruschenko A., Pochynyuk O., Booth R. E., Silverthorn D. U. (2008): Insight toward epithelial Na<sup>+</sup> channel mechanism revealed by the acid-sensing ion channel 1 structure. *IUBMB Life* **60**, 620–628  
<http://dx.doi.org/10.1002/iub.89>
- Takeda A. N., Gautschi I., van Bemmelen M. X., Schild L. (2007): Cadmium trapping in an epithelial sodium channel pore mutant. *J. Biol. Chem.* **282**, 31928–31936  
<http://dx.doi.org/10.1074/jbc.M700733200>
- Thevenod F., Lee W. K. (2013): Toxicology of cadmium and its damage to mammalian organs. *Met. Ions Life Sci.* **11**, 415–490  
[http://dx.doi.org/10.1007/978-94-007-5179-8\\_14](http://dx.doi.org/10.1007/978-94-007-5179-8_14)
- Thompson M. A. (2004) Molecular docking using ArgusLab, an efficient shape-based search algorithm and the AScore scoring function, in 228th ACS National Meeting, Philadelphia, PA
- Tsuruoka S., Swenson E. R., Fujimura A., Imai M. (2008): Mechanism of Cd-induced inhibition of Na-glucose cotransporter in rabbit proximal tubule cells: roles of luminal pH and membrane-bound carbonic anhydrase. *Nephron Physiol.* **110**, p11–20  
<http://dx.doi.org/10.1159/000161986>
- Van Driessche W., Erlj D. (1991): Cyclic AMP increases electrical capacitance of apical membrane of toad urinary bladder. *Arch. Int. Physiol. Biochim. Biophys.* **99**, 409–411
- Van Driessche W., Kreindler J. L., Malik A. B., Margulies S., Lewis S. A., Kim K. J. (2007): Interrelations/cross talk between transcellular transport function and paracellular tight junctional properties in lung epithelial and endothelial barriers. *Am. J. Physiol. Lung Cell. Mol. Physiol.* **293**, L520–524  
<http://dx.doi.org/10.1152/ajplung.00218.2007>
- Vennekens R., Prenen J., Hoenderop J. G., Bindels R. J., Droogmans G., Nilius B. (2001): Pore properties and ionic block of the rabbit epithelial calcium channel expressed in HEK 293 cells. *J. Physiol.* **530**, 183–191  
<http://dx.doi.org/10.1111/j.1469-7793.2001.01831.x>
- Wagner C. A., Waldegger S., Osswald H., Biber J., Murer H., Busch A. E., Lang F. (1996): Heavy metals inhibit Pi-induced currents through human brush-border NaPi-3 cotransporter in Xenopus oocytes. *Am. J. Physiol.* **271**, F926–930
- Yang H., Yu Y., Li W. G., Yu F., Cao H., Xu T. L., Jiang H. (2009): Inherent dynamics of the acid-sensing ion channel 1 correlates with the gating mechanism. *PLoS Biol.* **7**, e1000151  
<http://dx.doi.org/10.1371/journal.pbio.1000151>
- Yu L., Eaton D. C., Helms M. N. (2007): Effect of divalent heavy metals on epithelial Na<sup>+</sup> channels in A6 cells. *Am. J. Physiol. Renal Physiol.* **293**, F236–244  
<http://dx.doi.org/10.1152/ajprenal.00002.2007>
- Zhou Y., Xia X. M., Lingle C. J. (2015): Cadmium-cysteine coordination in the BK inner pore region and its structural and functional implications. *Proc. Natl. Acad. Sci. U.S.A.* **112**, 5237–5242  
<http://dx.doi.org/10.1073/pnas.1500953112>

Received: July 9, 2015

Final version accepted: November 23, 2015

First published online: April 5, 2016

## Supplementary Material

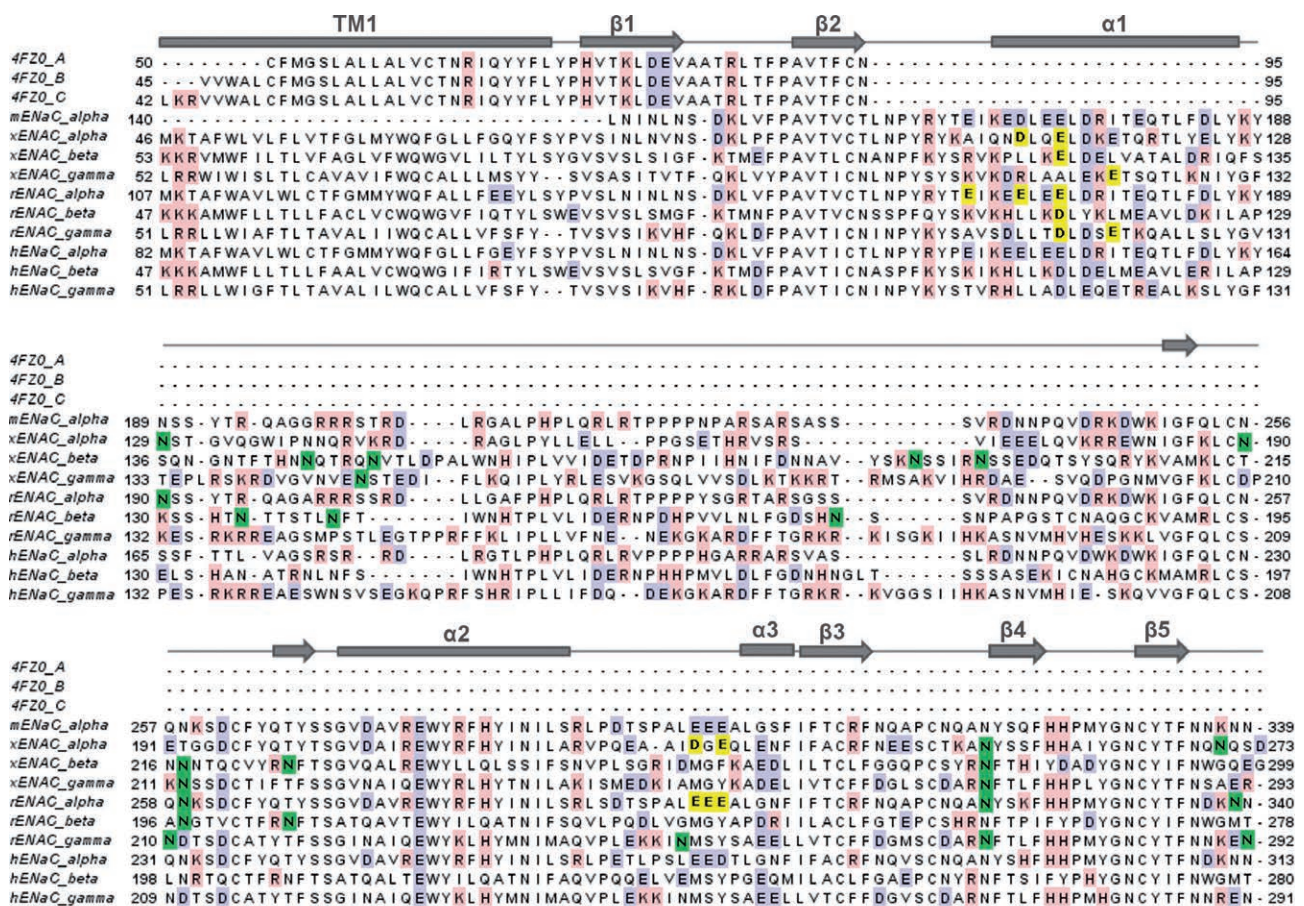
Effects of Cd<sup>2+</sup> on the epithelial Na<sup>+</sup> channel (ENaC) investigated by experimental and modeling studies

Maria Mernea<sup>1</sup>, Roxana Ulăreanu<sup>1</sup>, Octavian Călborean<sup>1</sup>, Sergiu Chira<sup>2</sup>, Octavian Popescu<sup>2</sup>, Dan F. Mihailescu<sup>1</sup> and Dana Cucu<sup>1</sup>

<sup>1</sup> Department of Anatomy, Physiology and Biophysics, Faculty of Biology, University of Bucharest, Bucharest, Romania

<sup>2</sup> Molecular Biology Centre, Institute for Interdisciplinary Experimental Research, University "Babes-Bolyai", 42 August Treboniu Laurean, 400271 Cluj-Napoca, Romania

## Supplementary Figures



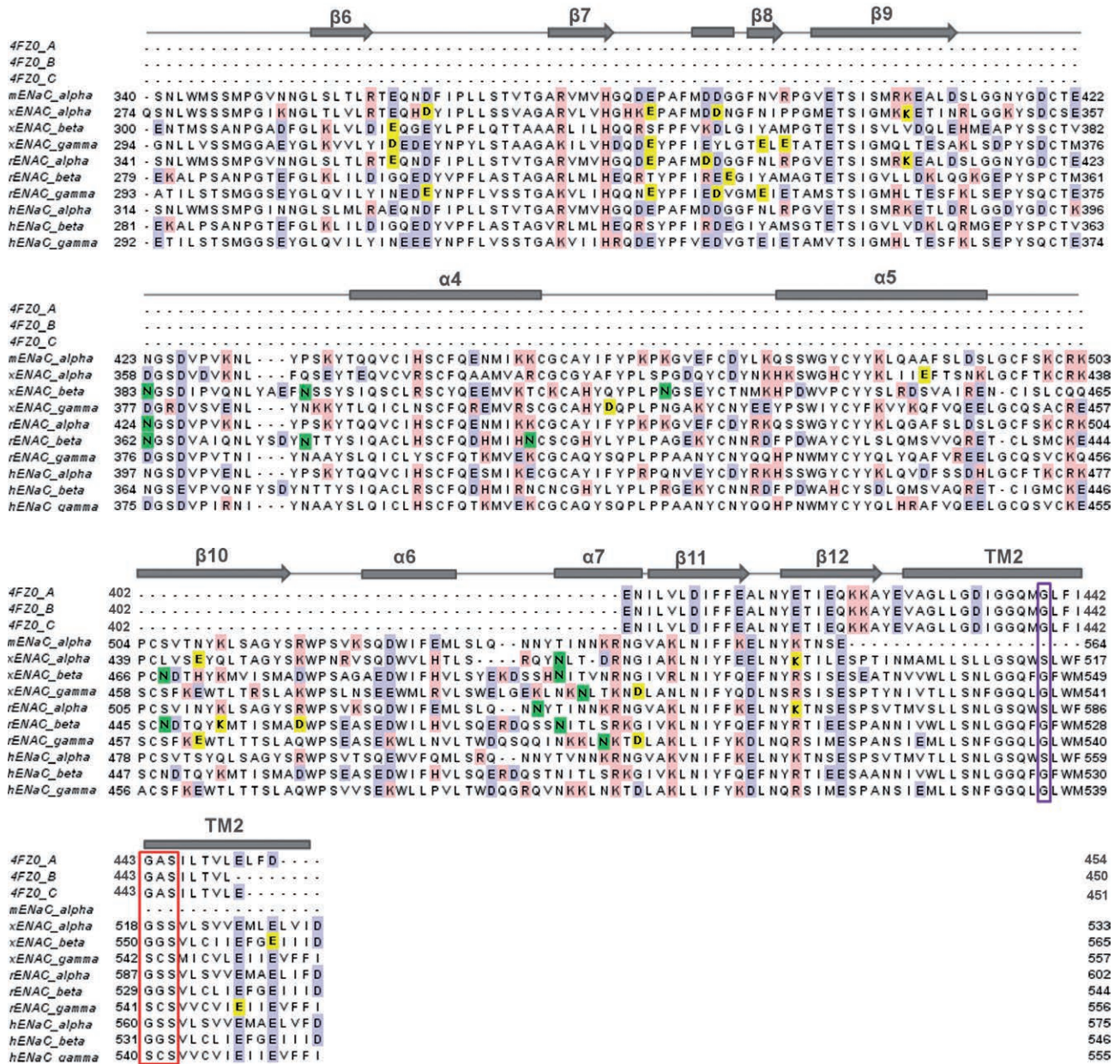


**Figure S1.** Sequence alignment between xENaC, rENaC and hENaC subunits with the templates used for modeling the channels: the amino- and carboxi- regions of ASIC1 subunits from the crystal structure 4FZ0. The sequences used to model TM regions f are denoted 4FZ0\_A, 4FZ0\_TM\_B and 4FZ0\_TM\_C. The extracellular domain of a mouse, denoted as mENaC, was used to model the extracellular loops and built with a long  $\alpha 2$  helix. The amino acids from the sequences are colored according to their electrical charge: light blue for negatively charged residues and pink for positively charged ones. The glycosylation sites present in rat and Xenopus ENaC models are colored in green, and the neutral Asp, Glu and Lys residues at pH 7.4 are in yellow. The selectivity filters of ENaC and ASIC are circled in red, whereas the putative amiloride binding sites found near the selectivity filters are shown as purple circles. The secondary structures present in rENaC and xENaC are presented above of each sequence.

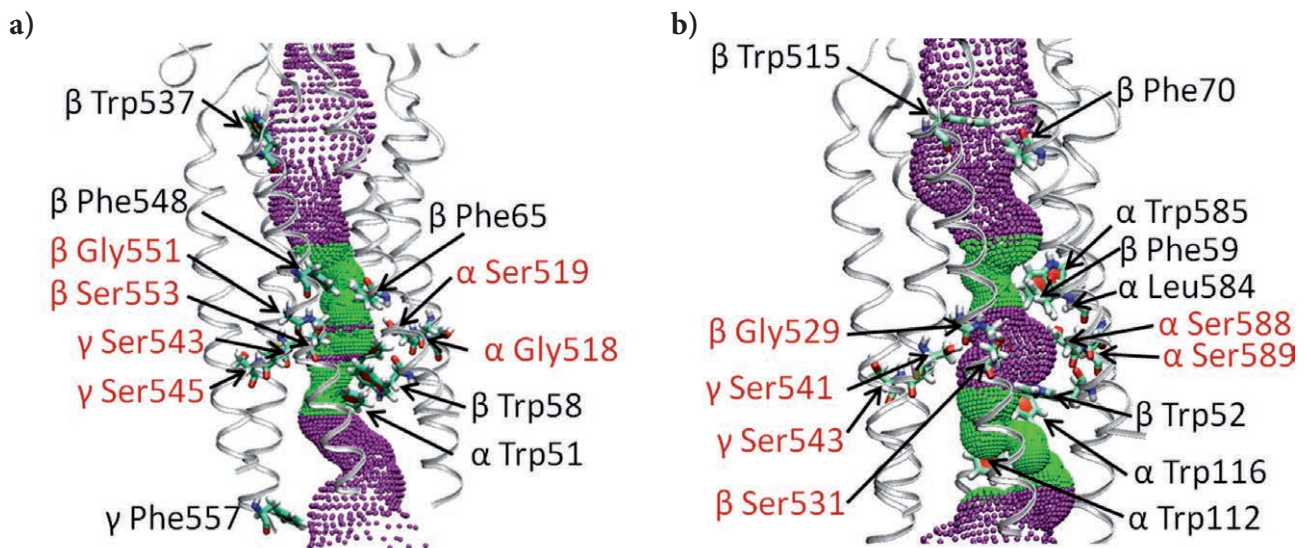


**Figure S2.** The transmembrane region of the xENaC channel pore is shown in (a) and the transmembrane region of rENaC in (b). The solvent-accessible pathways are colored green in the regions where the pore radius is between 1.4 Å and 2.5 Å and purple in regions where the pore radius exceeds 2.5 Å. The hydrophobic residues whose side chains protrude inside the channel pores and contribute in shaping the solvent-accessible pathways are labeled. The amino acids that form the selectivity filters of the channels are also represented on the figure and labeled in red.

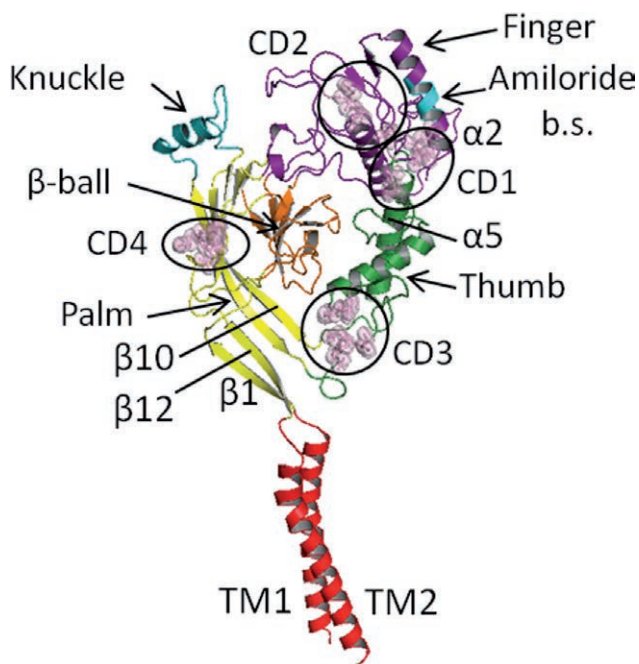


**Figure S3.** Structure of an  $\alpha$  xENaC subunit. The structural domains are labeled and colored using the same coloring scheme presented earlier. The secondary structures that present high fluctuations during the first 250 normal modes are labeled. Residues that form Cd<sup>2+</sup> binding sites are represented using pink spheres and labeled according to the distance from the amiloride binding site, shown in cyan.